Energy deposition of H and He ion beams in hydroxyapatite films: A study with implications for ion-beam cancer therapy

Silvina Limandri,[1] Pablo de Vera,[2] Raul C. Fadanelli,[3] Luiz C. C. M. Nagamine,[4] Alexandre Mello,[5] Rafael Garcia-Molina,[6] Moni Behar,[3] and Isabel Abril[2,*]

[1]*Centro Atómico Bariloche, RA-8400 San Carlos de Bariloche, Argentina*
[2]*Departament de Física Aplicada, Universitat d'Alacant, E-03080 Alacant, Spain*
[3]*Instituto de Física, Universidade Federal do Rio Grande do Sul, Porto Alegre, 91501-970, Brazil*
[4]*Instituto de Física, Universidade de São Paulo, 05508-090, São Paulo, Brazil*
[5]*Centro Brasileiro de Pesquisas Físicas, Rua Dr. Xavier Sigaud, 150, Rio de Janeiro, 22290-180, RJ, Brazil*
[6]*Departamento de Física, Centro de Investigación en Óptica y Nanofísica, Regional Campus of International Excellence "Campus Mare Nostrum," Universidad de Murcia, E-30100 Murcia, Spain*

(Received 5 November 2013; published 3 February 2014)

Ion-beam cancer therapy is a promising technique to treat deep-seated tumors; however, for an accurate treatment planning, the energy deposition by the ions must be well known both in *soft* and *hard* human tissues. Although the energy loss of ions in water and other organic and biological materials is fairly well known, scarce information is available for the *hard* tissues (i.e., bone), for which the current stopping power information relies on the application of simple additivity rules to atomic data. Especially, more knowledge is needed for the main constituent of human bone, calcium hydroxyapatite (HAp), which constitutes 58% of its mass composition. In this work the energy loss of H and He ion beams in HAp films has been obtained experimentally. The experiments have been performed using the Rutherford backscattering technique in an energy range of 450–2000 keV for H and 400–5000 keV for He ions. These measurements are used as a benchmark for theoretical calculations (stopping power and mean excitation energy) based on the dielectric formalism together with the MELF-GOS (Mermin energy loss function-generalized oscillator strength) method to describe the electronic excitation spectrum of HAp. The stopping power calculations are in good agreement with the experiments. Even though these experimental data are obtained for low projectile energies compared with the ones used in hadron therapy, they validate the mean excitation energy obtained theoretically, which is the fundamental quantity to accurately assess energy deposition and depth-dose curves of ion beams at clinically relevant high energies. The effect of the mean excitation energy choice on the depth-dose profile is discussed on the basis of detailed simulations. Finally, implications of the present work on the energy loss of charged particles in human cortical bone are remarked.

DOI: 10.1103/PhysRevE.89.022703 PACS number(s): 87.53.−j, 87.50.−a, 34.50.Bw, 87.85.jc

I. INTRODUCTION

Cancer therapy with ion beams is an outstanding and efficient technique to treat deep-seated tumors, which is rapidly spreading worldwide due to its excellent clinical results in comparison to conventional treatment using photon or electron radiation [1–5]. The main advantage of ion beams is that their energy deposition rate is maximum at the end of their range and not near the tissue surface as it happens with photons and electrons. The characteristic depth-dose profile of the ions has a sharp maximum (called Bragg peak), thus the use of ion beams in cancer therapy allows an accurate irradiation of the tumor with minimum collateral damage in surrounding healthy tissue.

To control the (desirable as well as undesirable) effects produced in biological tissues by an energetic ion beam it is necessary to gain insight in the depth-dose deposition, as well as in the cellular DNA damage and its subsequent repair mechanisms. The complexity of ion-beam interactions with living matter makes it difficult to provide only experimental data sets for treatment planning, therefore theoretical models and simulation methods are indispensable to describe the relevant processes concerned in the biodamage by ion irradiation [6–8]. Recently a multiscale approach to tackle this intricate problem, where different events happen on many spatial, temporal, and energetic scales, has been proposed [9,10].

During its travel through the human body, energetic ion beams (with energies in the order of tens and hundreds of MeV/u) can sample different biological materials, which can be grouped, mainly into *soft* and *hard*. Generally it is assumed that soft tissues can be approximated as liquid water, and so far the experimental and (mainly) theoretical efforts have concentrated on this material. Due to the inherent difficulty of measuring stopping power data in liquid targets, most of the available experiments are for water vapor and ice, although some scarce measurements have been reported for liquid water too [11–17]. Several theoretical approaches exist to study the energy loss of charged particles in liquid water [18–22], which can account for the general trends observed in the experimental data. Even though controversial results about the experimental stopping power derived from a proton beam incident on a liquid water jet have recently been discussed [23]. Regarding other organic and biological materials present in *soft* tissues, an empirical parametrization for obtaining their excitation spectrum has been proposed, which allows an accurate calculation of their stopping powers [24].

*Corresponding author: ias@ua.es

Contrary to the experimental and theoretical evidence existing for liquid water and *soft* tissues, less information is available for the stopping of charged particles in *hard* tissues, bone being the most representative. So far the main source of stopping power for ion beams in bone is the additivity of atomic stopping powers [25,26], since experimental data are very scarce [27,28]. Moreover, bone being a natural composite of collagen protein and mineral hydroxyapatite [29], no experimental data exist for the stopping power of its main constituent, which is calcium hydroxyapatite (HAp), with stoichiometric formula $Ca_{10}(PO_4)_6(OH)_2$ [30–32].

Apart from being the main constituent (58%) in mass of human bone [30], HAp properties render it as an appropriate bioactive material for safe, effective, and reliable use within a physiological environment [33]. Thanks to its inherent biocompability, synthetic HAp forms a strong bond with human bone and is considered a significant biomaterial due to its potential medical applications for bone replacement or implants [34–37].

Despite the intrinsic interest of HAp as a biomaterial and as the main constituent of bone, there are no experimental data of its stopping power for energetic ion beams, which is necessary to provide basic information on the energy loss of charged particles in bone, and in order to obtain reliable accurate depth-dose distributions necessary in ion-beam cancer therapy [38,39]. In particular, knowing the precise value of the mean excitation energy I of HAp (and bone) is strongly desirable, since this magnitude is the main target-dependent ingredient in the Bethe formula [40], which is extensively used for range determinations with submillimeter precision [41].

The present work reports experimental measurements of the stopping power of HAp for H and He ion beams, together with theoretical calculations based on the dielectric formalism, which successfully reproduce these measurements and provide a reliable value of the mean excitation energy I of HAp, since it is based on its electronic excitation spectrum. This information is used to calculate the stopping power and the mean excitation energy of human cortical bone.

This paper is structured as follows. In Sec. II we present the preparation procedure of the HAp thin films and their characterization by the grazing-incidence x-ray diffraction technique. In Sec. III we describe the experimental procedure to measure the stopping power of HAp thin films for H and He ions by means of the Rutherford backscattering technique for a broad incident energy interval. Theoretical calculations based on the dielectric formalism, together with the MELF-GOS method [42,43] to describe the electronic excitation spectrum of the HAp, are presented in Sec. IV. The calculated stopping power is compared with the experimental data in Sec. V, where the value of the mean excitation energy of HAp is obtained. The influence of using this mean excitation energy, instead of the one derived by applying a simple additivity rule, in the depth-dose profiles of H and He ion beams in HAp is examined by means of the simulation code SEICS (simulation of energetic ions and clusters through solids) [44]. In Sec. VI our findings for HAp are applied to discuss the energy loss of ion beams in cortical bone, and the summary of this work is presented in Sec. VII.

II. PREPARATION AND CHARACTERIZATION OF THE HAp THIN FILMS

Powdered stoichiometric hydroxyapatite $Ca_{10}(PO_4)_6(OH)_2$ was produced at the Brazilian Center for Physics Research as described elsewhere [45]. Briefly, stoichiometric HAp powder (Ca/P ratio = 1.67) was synthesized from the drop wise addition of calcium nitrate and ammonium phosphate solutions at 37 °C (all p.a. reagents from Merck). The pH was kept at approximately 9 by the addition of KOH. After 2 h of sintering, the precipitate was separated by filtration and repeatedly washed with cold deionized water (Mili-Q brand). The suspension was lyophilized and the dried powder was ground. Particles diameters inferior to 210 μm were separated by sieving. HAp sputtering target disks with a diameter of 25 mm and a thickness of 3 mm were prepared by 30 MPa uniaxial pressing of the HAp powder, followed by 2 h sintering at 1100 °C, reached by a rising of 10 °C/min and further cooling inside the furnace.

The magnetron sputtering technique at suitable right angle geometry was chosen, since the backsputtering effects which lead to lack of oxygen and structural disorder on the as-sputtered films were reduced and stoichiometry and crystallinity can be improved in these films [46–48]. For all thin films' deposition, the sputtering gas used was a mixture of ultrahigh purity argon and oxygen with partial pressures set at 6.66×10^{-1} Pa (5 mTorr) and 1.33×10^{-1} Pa (1 mTorr), respectively. The base pressure of the chamber was lower than 1.33×10^{-4} Pa (10^{-6} Torr). The rf power at 120 W was applied to the two opposing targets through an impedance matching π network. HAp films with nominal thicknesses of 19, 37, 60, 81, 102, and 151 nm were grown onto amorphous carbon substrates. A thicker HAp film (733 nm) was also deposited on a Si(100) substrate to be characterized by the grazing incidence x-ray diffraction (GIXRD). The thicknesses and a mean density of 3.22 g/cm^3, in good agreement with other reported values [32], were obtained by using the software package WINGIXA by Philips [49,50] to fit the x-ray specular reflectivity (XRR) curves obtained in a Rigaku diffractometer.

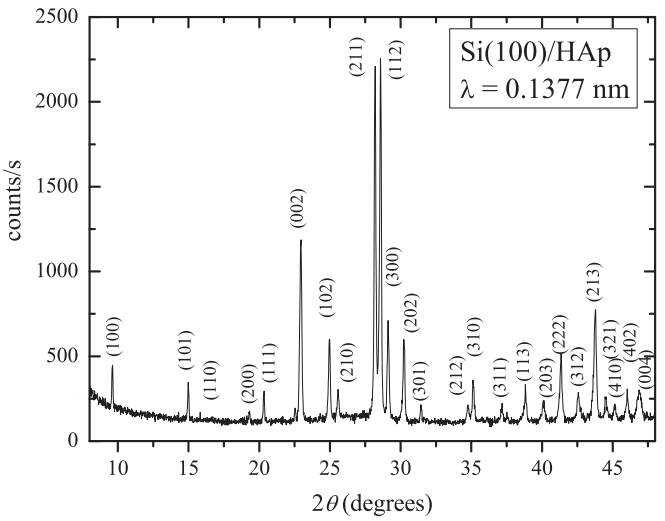

FIG. 1. Synchrotron radiation x-ray diffraction pattern for a 733 nm thick HAp film deposited onto a Si(100) substrate.

The phase composition of the HAp thin films was characterized by GIXRD [48] at the Brazilian Synchroton Light National Laboratory, operating at 9 keV corresponding to a wavelength of 0.1377 nm, fixed incident angle $\theta = 0.5°$ and 1°, diffracted 2θ angle scanned in the range of 9° to 50° at a rate of 0.04°/point s^{-1}. The x-ray pattern obtained on the thicker HAp film (733 nm) deposited onto a Si(100) substrate is shown in Fig. 1. All peaks were indexed to a pure HAp according to the ICCD-PDF#00-009-0432 database. Some strongly preferred orientations for the (100) and (002) planes are usually found for HAp sputtered thin films [51]. For the thicker film of this work, the GIXRD pattern also shows higher relative intensities (I_{hkl}/I_{211}) as compared to the ones found in the ICCD database. Preferred crystal growth could be attributed to the sputtering process and mainly to the low growing energy of those main HAp crystallographic planes.

III. EXPERIMENTAL ENERGY LOSS OF H AND He ION BEAMS IN HAp FILMS

The energy losses of H and He ion beams in HAp were determined by means of the Rutherford backscattering technique (RBS) using the beams provided by the 500 kV ion implanter (for the lower energies) and the 3 MV Tandetron accelerator (for the higher ones). These experiments were performed at the Instituto de Física da Universidade Federal do Rio Grande do Sul, Brazil.

The energy of the H beam covered in the present experiment was between 450 and 2000 keV; the total detector plus electronic resolution was better than 7 keV. For the He beam case, the investigated energy ranges from 400 up to 5000 keV and the combined electronic plus detector energy resolution was better than 12 keV.

The target sample was mounted on a four-axis goniometer and the position of the detector was fixed at 120° with respect to the beam direction. For each incident energy, the angle between the beam and the normal to the sample was varied between 0° and 60°, in steps of 20°. In Fig. 2 a typical RBS spectrum obtained with a 3 MeV He beam impinging on a 151 nm film is shown. As can be observed the signals of the Ca, P, and O elements of the HAp matrix can be clearly distinguished. The selection of the sample thicknesses was done according to the beam energy. In some cases, for the same energy, two samples with different thicknesses were used and the corresponding results were quite similar. In addition, for He at higher energies, when the signals of the Ca and P components were well separated, the stopping values were determined from these elements. However, for energies lower than 1 MeV, the above elements collapsed into one peak. In this case, the O signal was used to determine the low-energy stopping power values.

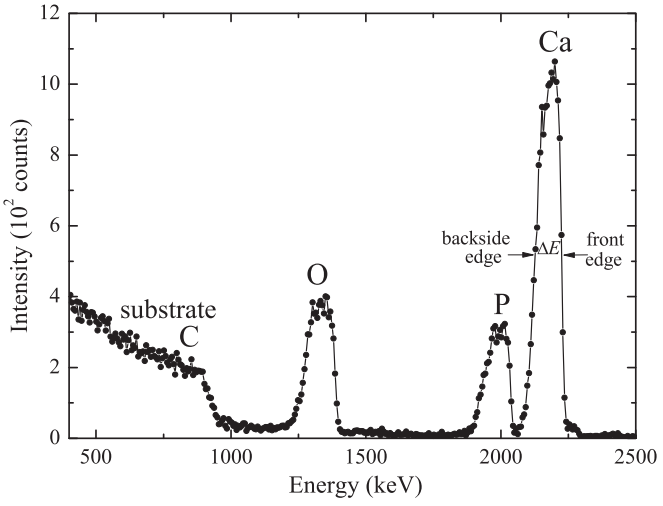

FIG. 2. Rutherford backscattering spectrum resulting from a 151 nm HAp film placed at normal incidence with respect to a 3 MeV He^+ beam.

The energy loss ΔE of the H and He ions in a HAp sample was evaluated by determining the position of both the front and back edges of the corresponding RBS energy distribution (either Ca and P, or O, as previously mentioned). As discussed in Ref. [52] we have used the error function and the complementary error functions to fit both the back side and the front side of the distributions, respectively. The experimental energy loss factor $\Delta E/x$ for the ions backscattered at a depth x of the film is related to the stopping power through the following relation based on the mean-energy approximation [53]:

$$\frac{\Delta E}{x} = \frac{K}{\cos\theta_1}\frac{dE}{dx}(\bar{E}_{\rm in}) + \frac{1}{\cos\theta_2}\frac{dE}{dx}(\bar{E}_{\rm out}), \qquad (1)$$

where $\frac{dE}{dx}(\bar{E})$ is the stopping power at the energy $\bar{E}$, K is the kinematic (or Rutherford energy loss) factor, $\bar{E}_{\rm in}$ and $\bar{E}_{\rm out}$ are, respectively, the energies along the inward and outward paths, whereas θ_1 and θ_2 are the angles of the sample normal with respect to the incoming beam and to the detector direction, respectively. Considering Eq. (1) for ions backscattered at the back of the HAp film, with x equal to the film thickness, when measuring at two (or more) different geometries, a system of equations is obtained which can be solved to get the stopping power values at energies $\bar{E}_{\rm in}$ and $\bar{E}_{\rm out}$. Four measurements were performed under different geometrical conditions ($\theta_1 =$ 0°, 20°, 40°, and 60°). The stopping powers were obtained at $\bar{E}_{\rm in} = (E + E_0)/2$ and $\bar{E}_{\rm out} = (KE + E_1)/2$, where E_0 is the energy of the incident particles, E is the energy immediately before scattering at a depth x, and E_1 is the energy of the backscattered particles emerging from the surface. For each angle, E was determined using the energy-loss ratio method as described in [53], giving four values for $\bar{E}_{\rm in}$ and $\bar{E}_{\rm out}$. The values used in Eq. (1) were the average of the individual results. The mean source of error is due to the dispersion between the different values obtained for a fixed energy at different angles and film thicknesses.

IV. THEORETICAL ENERGY LOSS CALCULATIONS

Fast heavy charged particles traveling through biomaterials deposit mainly their kinetic energy by inelastic interactions with the target electrons. An appropriate framework to describe the electronic energy loss of swift ions through a condensed medium is provided by the dielectric formalism [54–56]. For a projectile with atomic number Z and mass M, which travels with energy E through a medium characterized by a dielectric function $\varepsilon(k,\omega)$, the mean energy loss per length unit, namely,

the stopping power S, is given by

$$S(E) = \frac{e^2 M}{\pi E} \sum_{q=0}^{Z} \phi_q(E) \int_0^{\infty} \frac{dk}{k} [Z - \rho_q(k)]^2 \times \int_0^{k\sqrt{2E/M}} d\omega\, \omega \mathrm{Im}\left[\frac{-1}{\varepsilon(k,\omega)}\right], \quad (2)$$

where $\hbar k$ and $\hbar\omega$ represent the momentum and energy transferred to the target in an inelastic collision. The summation is performed over all the possible charge states q of the projectile, characterized by the Fourier transform $\rho_q(k)$ of its electronic density, which is described by the Brandt-Kitagawa model [57,58]. ϕ_q are the equilibrium charge state fractions of the projectile, which depend on its energy and the target nature; we have used in this work a parametrization to experimental data [59].

The target electronic excitation spectrum enters in the above expression through its energy loss function (ELF) $\mathrm{Im}[-1/\varepsilon(k,\omega)]$, which gives the probability to produce an excitation or ionization with energy $\hbar\omega$ and momentum $\hbar k$, i.e., the so-called Bethe surface. We calculate the ELF by using the MELF-GOS (Mermin energy loss function-generalized oscillator strengths) method [42,43], where a separation between the inner-shell and the outer-electron excitations is made, due to their different response to the perturbation induced by the projectile. The inner-shell electron excitations present large binding energies, therefore preserving their atomic character. They are described by the generalized oscillator strengths (GOS) in the hydrogenic approach [60]. For HAp films we consider as inner shells the K and L shell of Ca and P, and the K shell of O. The excitations of the weakly bound outer electrons are built from the available experimental ELF data at the optical limit ($\hbar k = 0$), through a fitting procedure by a weighted sum of Mermin-type ELF [61] as described in [43,62]. Proceeding in this manner we account for collective excitations as well as chemical and aggregation effects characteristics of the condensed media. The Mermin-ELF also incorporates plasmon damping through phonon assisted electronic transitions, which accounts for the finite plasmon lifetime and provides an analytic and realistic extension to finite momentum transfers [63].

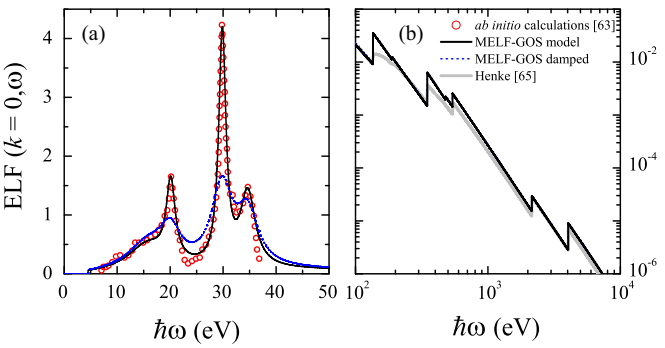

FIG. 3. (Color online) Energy loss function (ELF) of HAp at the optical limit ($\hbar k = 0$) at (a) low and (b) high energy transfer $\hbar\omega$. The *ab initio* DFT calculations [64] are shown by circles and their fitting by the MELF-GOS model [42,43] by a solid line. A phenomenological damped ELF is represented by a blue dashed line. The ELF at high energy transfer obtained from experimental scattering factors [66] is shown by a gray line in (b).

TABLE I. Parameters ω_i, γ_i, and A_i used to fit the *ab initio* calculated ELF of HAp [64] by a weigthed sum of Mermin-type ELF at the optical limit [42,43].

i	ω_i(eV)	γ_i(eV)	A_i
1	16.33	9.03	0.085
2	20.14	2.04	0.075
3	29.86	1.63	0.26
4	34.69	3.40	0.2
5	54.42	81.63	0.37

The MELF-GOS methodology only needs the optical-ELF as necessary input to find the Bethe surface of the target. Unfortunately, experimental optical-ELF data for HAp are not available; therefore we rely on *ab initio* calculations of the optical properties of HAp [64], based on the density functional theory (DFT) within the local-density approximation, which is particularly effective for systems with complex structures, as it is the case of HAp. The calculated ELF of HAp in the optical limit as a function of the transferred energy $\hbar\omega$, depicted in Fig. 3(a) by circles [64], presents a well-defined plasma frequency peak at 20 eV and another strong single peak near 30 eV. However, Rulis *et al.* [64] point out that the accuracy of the peak at 35 eV is questionable, because the Kramers-Kronig conversion to obtain the real part of the dielectric function from its imaginary part was done over a finite data set, therefore the final peak may be an artifact of that process. This calculated ELF has been fitted by a sum of five Mermin-ELF (solid line), with the fitting parameters shown in Table I, where ω_i, γ_i, and A_i correspond to the position, width, and height of each one of the Mermin-type ELF that has been used; a threshold energy of 4.5 eV was considered. Since the *ab initio* calculation of the ELF of HAp [64] does not take into account the atomic vibrations and the defects present in the real HAp, which would widen the peaks of the calculated ELF, we also present a phenomenological ELF of HAp (blue dashed line) with damped peaks with respect to the *ab initio* calculations, to take into account these facts and to check its influence in the stopping of projectiles in HAp. The width of the peaks in the phenomenological ELF is taken as $\gamma_i = 4.76$ eV for $i = 2 - 4$, whereas ω_i and A_i are the same as in the *ab initio* fitting ELF (see Table I). For both fitted ELFs, the fulfilment of the f-sum rule [65] is better than 99%. Figure 3(b) depicts the ELF of HAp at high transferred energies, where the calculated ELF (solid line) is compared with the ELF (gray line) obtained from experimental scattering factors [66], which provides the refractive index and the extinction coefficient for each atomic constituent of the HAp.

V. RESULTS AND DISCUSSION

In Fig. 4 we show by circles our measured stopping power of HAp for a H beam, as a function of the incident energy. The theoretical results, obtained as described previously, are also included. No significant differences have been found between the stopping power obtained with Eq. (2) from the ELF fitted to the *ab initio* calculations [64] (solid line)

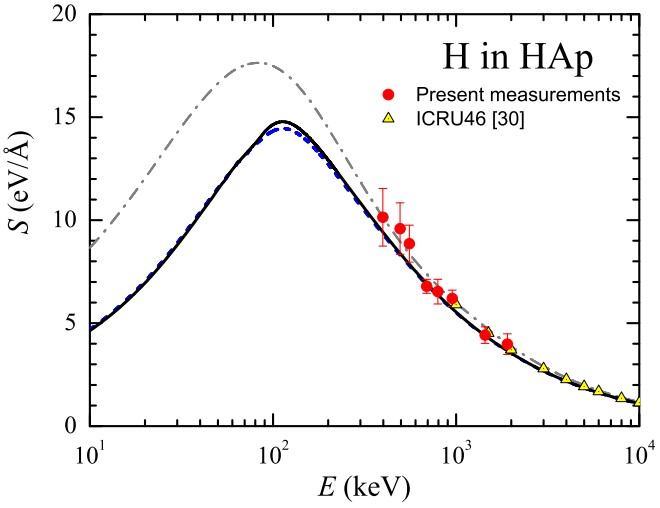

FIG. 4. (Color online) Experimental stopping power (circles) of HAp for a proton beam, as a function of the incident energy. Theoretical calculations obtained by the dielectric formalism and the MELF-GOS method from the *ab initio* ELF (solid line) and from a phenomenological damped ELF (dashed line) are also presented. Triangles are data for mineral bone from ICRU Report 46 [30] and the gray dash-dotted line corresponds to the predictions of the SRIM code [67].

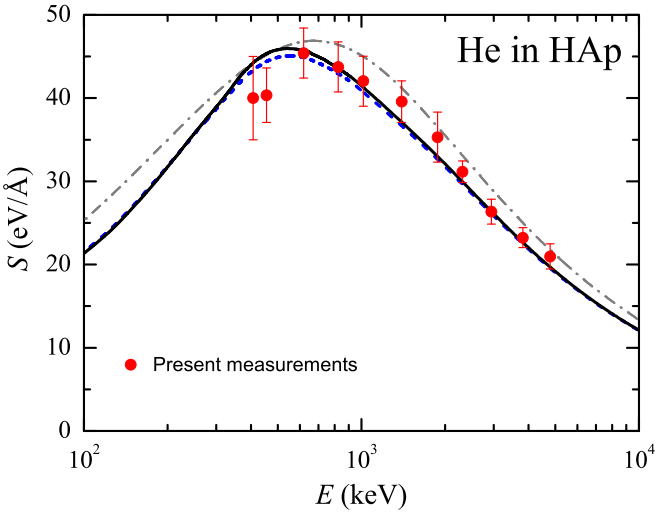

FIG. 5. (Color online) Experimental stopping power (circles) of HAp for a He ion beam, as a function of the incident energy. Theoretical calculations obtained by the dielectric formalism and the MELF-GOS method from the *ab initio* ELF (solid line) and from a phenomenological damped ELF (dashed line) are shown. Predictions by the SRIM code [67] are depicted by a gray dash-dotted line.

and from the phenomenologically damped ELF (dashed line), which confirm the appropriate choice of the ELF for HAp. The agreement between the experimental measurements and theoretical calculations is quite good within the error bars. The data from ICRU Report 46 [30] corresponding to mineral bone are depicted by triangles, which also are well reproduced by our calculations. The semiempirical predictions of the SRIM code [67] are shown by a gray dash-dotted line.

At high proton energies, the experimental stopping power values are compatible with those provided by the different models. However, as the proton energy decreases differences between the stopping power obtained from the MELF-GOS model and from the SRIM code [67] appear, presumably because an accurate description of the target electronic excitation spectrum is then necessary. In any case, more experimental data below and around the maximum stopping power are desirable.

The experimental stopping power of HAp for the He ion beam is shown by circles in Fig. 5, where energies around and larger than for the maximum stopping power have been explored. The theoretical results obtained from the dielectric formalism and the MELF-GOS model corresponding to the *ab initio* ELF (solid line) and to the phenomenological damped ELF (dashed line) have been included, which present similar values in all the energy range analyzed. The agreement for the He ion beam between the experimental stopping data and the calculated results is rather good, in particular around the maximum stopping power. The semiempirical SRIM predictions [67] are again included by a gray dash-dotted line.

Realistic clinical situations use ion beams with high initial energy ($\sim$100 MeV/u), where the stopping power is well described by the relativistic Bethe theory [40,68]:

$$S_{\mathrm{Bethe}} = \frac{4\pi e^4 Z^2 Z_t N}{v^2}\left(\ln\left\{\frac{2mv^2}{I[1-(v/c)^2]}\right\} - (v/c)^2\right), \tag{3}$$

where v and c are, respectively, the projectile and the light velocity, Z_t is the target atomic number, and I is the mean excitation energy of the target, which is the fundamental quantity for an accurate calculation of the stopping power. The value of I for each target depends on its electronic excitation spectrum, through the following relation [68,69]:

$$\ln I = \frac{\int_0^\infty d\omega\, \omega \ln\omega\, \mathrm{Im}[-1/\varepsilon(k=0,\omega)]}{\int_0^\infty d\omega\, \omega\, \mathrm{Im}[-1/\varepsilon(k=0,\omega)]}. \tag{4}$$

From this expression a straightforward calculation of I from the ELF is obtained from the MELF-GOS methodology, for any type of material. For HAp we obtain $I = 159.5$ eV and $I = 162.5$ eV, respectively, from the *ab initio* ELF calculation [64] and from the phenomenological damped ELF. These values for I are supported by the fact that the stopping power obtained at intermediate energies with this model agrees well with the experimental data for H and He ion beams (as shown in Figs. 4 and 5), which means that the ELF of HAp we are using is a good representation of its electronic excitation spectrum. However, the I value of HAp we obtain by applying Bragg's rule [25] from each HAp component is 140.2 eV. Since the indetermination in the I value of HAp will influence the energy deposition profile of ion beams as a function of the penetration depth in the material [41], we use the SEICS (simulation of energetic ions and clusters through solids) code [44,70] to obtain the depth-dose profile of H and He ion beams in HAp for different values of I.

The SEICS code, based on molecular dynamics and Monte Carlo techniques, simulates the trajectory of the incident

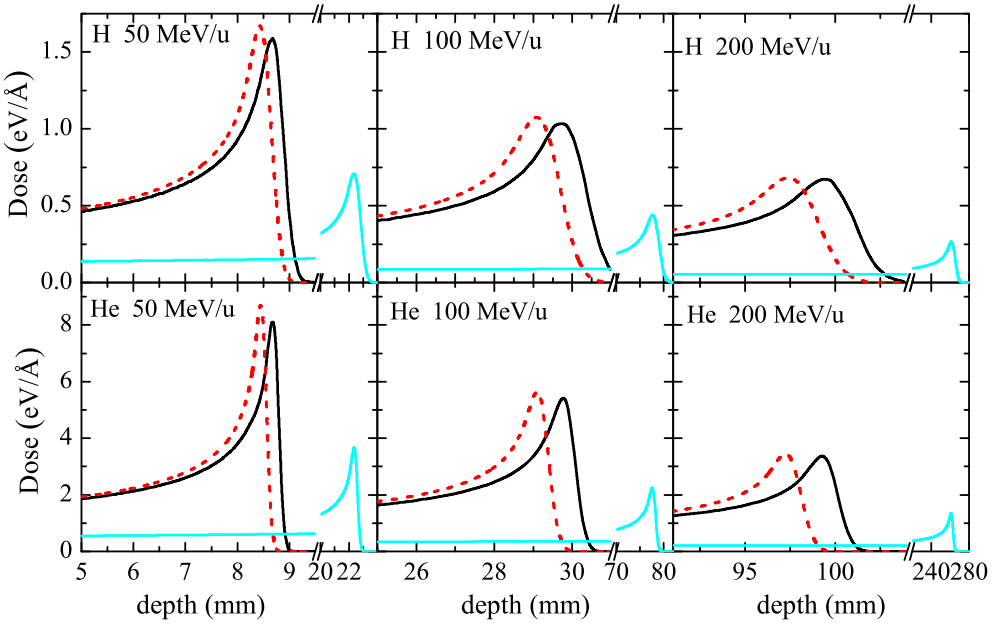

FIG. 6. (Color online) Depth-dose distributions of H and He ion beams in HAp, obtained with the SEICS code [44,70] at several energies, using our calculated I value (162.5 eV, black solid lines) and the I value obtained applying Bragg's rule (140.2 eV, red dashed lines). Note the difference depth scales for each incident energy (which is indicated in each panel). Depth-dose distributions of H and He ion beams in liquid water are shown by cyan solid lines (notice the break at the depth axis).

projectile inside the target by solving its equation of motion [44,70]. The following physical processes are considered: (i) electronic interactions with the target electrons (ionization and excitation), which are the main channel of energy transfer to the target (with statistical fluctuations around the mean value taken into account); (ii) elastic collisions with the target nuclei, which are responsible of the projectile trajectory deviations and the elastic energy loss; and (iii) dynamical charge-changing processes of the projectile. The input quantities in the code are the stopping power and the energy-loss straggling, which at projectile energies below 10 MeV/u are obtained as described in Sec. IV, and by the Bethe formula [Eq. (3)] at higher energies using the appropriate value of the mean excitation energy I.

In order to evaluate the influence of the mean excitation energy the simulated depth-dose distributions for H and He ion beams in HAp at several energies are shown in Fig. 6. Black solid lines represent the result of simulations performed using the calculated I value from the electronic excitation spectrum of HAp, 162.5 eV, whereas red dashed lines are obtained with the I value deduced from Bragg's rule, 140.2 eV. In the simulation, nuclear fragmentation reactions have not been included. We conclude that differences in the I values give variations in the position of the Bragg peak that are around 0.2–1.7 mm (2%–3%) for protons and 0.2–2 mm (2-%–3%) for He ion beams. For comparison purposes, we also include the depth-dose distributions in liquid water (cyan solid lines), for a I value of 79.4 eV [22].

VI. APPLICATIONS TO CORTICAL BONE

Although the experimental stopping power of HAp for H and He ion beams presented in Figs. 4 and 5 is worthy by itself, as HAp is a relevant biological material listed in ICRU Report 46, being 58% of the composition in mass of cortical bone [30], the experimental data and the theory reported in this work also allows the calculation of the energy loss of charged particles in cortical bone, a biomaterial that unavoidably appears due to heterogeneities [71,72] in many real treatment plannings.

Since we know the stopping power of the mineral part (HAp) of bone, we only need to obtain the stopping power of the remaining 42% of organic material. Then we find the bone stopping power from Bragg's rule applied to its mineral and organic parts. Since they can be regarded as different chemical phases, this approximation will lead to negligible errors.

The composition and density of the organic part of bone is obtained as follows. From the composition of cortical bone (density = 1.85 g/cm^3) given by the ICRU Report 49 [25], we assume that all its calcium content comes from the mineral part (i.e., HAp). Then we subtract the corresponding composition of HAp from that of cortical bone in order to obtain the composition of its organic part. The density of the latter (1.169 g/cm^3) was obtained from the densities of cortical bone, HAp, and the mass contents of HAp and organic part of cortical bone [25]. We summarize in Table II the compositions and densities of HAp, cortical bone, and its organic part. Once the composition and density of the organic part of bone is known, a parametrization for the optical-ELF of organic compounds [24] allows us to find its stopping power [Eq. (2)] and its mean excitation energy [Eq. (4)], which results in $I_{\text{organic part}} = 74.6$ eV.

Finally, we apply Bragg's rule to calculate the stopping power and I value of cortical bone from its mineral and organic constituents (note that Bragg's rule is applied to two different chemical phases, not to the atomic constituents of cortical bone as was suggested in the ICRU report [25]). In Fig. 7 we show the stopping cross section (SCS = S/density) of cortical bone

TABLE II. Composition, density, and mean excitation energy I of the materials studied in this work.

Material	Composition (% mass)[a] C	H	N	O	P	Ca	S	Density (g/cm^3)	$I_{\text{MELF-GOS}}$ (eV)	I_{ICRU} (eV)
HAp $Ca_{10}(PO_4)_6(OH)_2$	0.00	0.20	0.00	41.41	18.50	39.89	0.00	3.22	159.5–162.5	140.2
Organic part of cortical bone	30.46	9.74	8.87	48.18	1.62	0.00	1.13	1.165	74.6	–
Cortical bone [25]	14.43	4.72	4.20	44.61	10.50	20.99	0.32	1.85	113.9–115.0	106.4

[a]For simplicity, elements heavier than S with presence less than 1% have been omitted in the composition.

for H and He beams obtained, as was previously explained, as a function of the projectile energy (solid lines). Our findings are compared with the results obtained from the PSTAR code for H and from the ASTAR code for He (dashed lines) [26]. For the case of H projectiles we observe sizable differences at energies around and less than the maximum stopping power, whereas for He projectiles the differences are smaller. The SCS of HAp is also included in the figures as dotted lines, in order to quantify its contribution to the SCS of cortical bone.

The mean excitation energies of the materials discussed in this paper appear in the last two columns of Table II. Our model predicts for cortical bone a value of the mean excitation energy $I_{\text{MELF-GOS}} = 113.9$ and 115.0 eV, using the *ab initio* and damped ELF of HAp, respectively, while the value derived by applying an additivity rule to each atomic component [26] is $I_{\text{ICRU}} = 106.4$ eV. Our results compare quite well with the experimental mean excitation energy reported by Hiraoka *et al.* [28] for "hard bone" substitute (density = 1.826 g/cm^3), which is 114.0 eV. Moreover, an experimental mass stopping power ratio for 100 MeV protons in skull bone (with composition and density very similar to cortical bone) with respect to liquid water was reported to be 0.900 ± 0.005 [27]; at this energy our results yield a ratio of 0.894, which is in very good agreement with the experiment data. Therefore, an important outcome of the work reported in this paper for the stopping of H and He beams in HAp is the successful application to the calculation of the energy loss of charged particles in human cortical bone, whose presence intercepting the ion-beam path in cancer treatment planning must be properly taken into account.

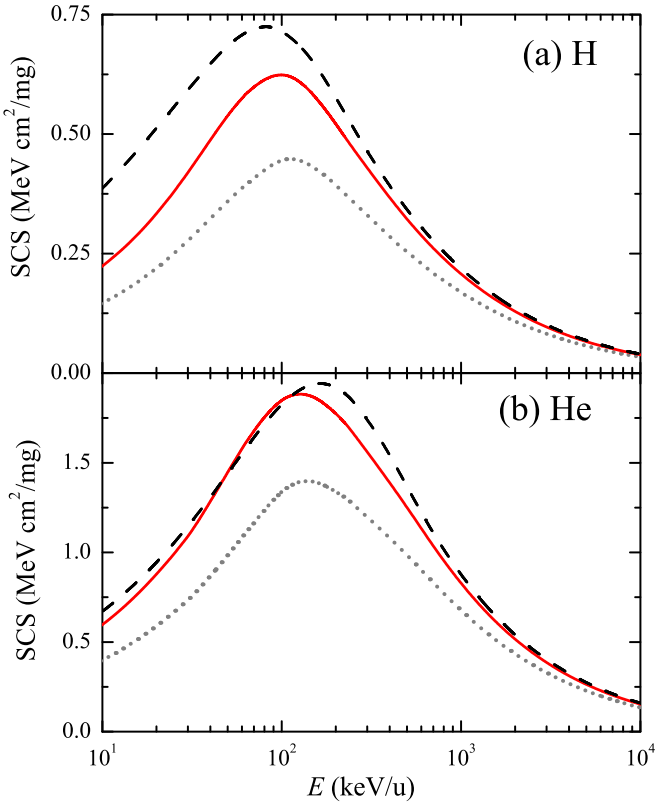

FIG. 7. (Color online) Stopping cross section (SCS) of cortical bone for (a) H and (b) He ion beams (solid line), obtained from the MELF-GOS model. The results obtained from the PSTAR code for H and the ASTAR code for He are shown by dashed lines [26]. For comparison purposes, the SCS of HAp is also presented by means of dotted lines.

VII. SUMMARY AND IMPLICATIONS

The experimental stopping power of HAp (the mineral part of bone) for H and He beams has been measured in a wide energy range by using the Rutherford backscattering technique. The corresponding theoretical calculations, derived from the dielectric formalism and a proper description of the HAp electronic excitation spectrum, show a nice agreement with the experimental data. This fact supports the value obtained for the mean excitation energy of HAp, which is 159.5–162.5 eV, significantly different from the value of 140.2 eV obtained from the application of Bragg's rule [25] to its atomic components. Depth-dose profiles of H and He in HAp have been obtained with the SEICS code to illustrate the non-negligible consequences in the choice of the mean excitation energy, especially relevant at higher incident energies (which are the more usual in ion cancer therapy).

Finally, the calculated stopping power of HAp for H and He ion beams has been used to estimate the stopping power in human cortical bone, making use of an empirical approach to calculate the ELF of its organic part, and by properly weighing the stopping powers of the mineral and organic parts of the bone. The I value obtained for cortical bone (113.9–115.0 eV) satisfactorily agrees with the experimental value (114.0 eV) for "hard bone" substitute [28], and yields a bone-water mass stopping power ratio for 100 MeV protons of 0.894, which is in excellent agreement with the experimental value of 0.900 ± 0.005 reported for skullbone [27].

In conclusion, we have shown how fundamental physics inspired studies, such as the one reported in this work, have implications in the field of ion-beam cancer therapy, where an accurate knowledge of the energy deposited by swift ions in different human tissues is required for a proper treatment planning.

ACKNOWLEDGMENTS

The authors wish to thank the Brazilian Synchrotron Light National Laboratory in Campinas, Brazil (LNLS) for the use of the GIXRD diffraction technique, the Crystallographic Laboratory of Physics Institute-USP for the use of the x-ray diffraction, and Professor Alexandre M. Rossi from CBPF-Brazil for providing the HAp powder material. This work has been financially supported by the Spanish Ministerio de Economía y Competividad and the European Regional Development Fund (Project FIS2010-17225) and the Brazilian agency CAPES (project CAPES-MinCyT 220/12). P.d.V. thanks the Conselleria d'Educació, Cultura i Esport de la Generalitat Valenciana for its support under the VALi+d program. This research has been developed as a part of the COST Action MP 1002, Nanoscale Insights into Ion Beam Cancer Therapy.

[1] G. Kraft, Prog. Part. Nucl. Phys. **45**, S473 (2000).
[2] M. Goitein, A. J. Lomas, and E. Pedroni, Phys. Today **55**, 45 (2002).
[3] A. Brahme, Int. J. Radiat. Oncol. Biol. Phys. **58**, 603 (2004).
[4] D. Schardt, T. Elsässer, and D. Schulz-Ertner, Rev. Mod. Phys. **82**, 383 (2010).
[5] Edited by D. Belkic, *Theory of Heavy Ion Collision Physics in Hadron Therapy*, Adv. Quantum Chem. (Elsevier, Amsterdam, 2013).
[6] H. Paganetti, H. Jiang, K. Parodi, R. Slopsema, and M. Engelsman, Phys. Med. Biol. **53**, 4825 (2008).
[7] H. Paganetti and H. Kooy, Expert Rev. Med. Devices **7**, 275 (2010).
[8] E. Surdutovich, D. C. Gallagher, and A. V. Solov'yov, Phys. Rev. E **84**, 051918 (2011).
[9] A. V. Solov'yov, E. Surdutovich, E. Scifoni, I. Mishustin, and W. Greiner, Phys. Rev. E **79**, 011909 (2009).
[10] E. Surdutovich, E. Scifoni, and A. V. Solov'yov, Mutation Res. **704**, 206 (2010).
[11] R. B. J. Palmer and A. Akhavan-Rezayat, J. Phys. D **11**, 605 (1978).
[12] A. Akhavan-Rezayat and R. B. J. Palmer, J. Phys. E **13**, 877 (1980).
[13] D. I. Thwaites, Phys. Med. Biol. **26**, 71 (1981).
[14] A. K. M. M. Haque, A. Mohammadi, and H. Nikjoo, Radiat. Protect. Dosim. **13**, 71 (1985).
[15] M. Shimizu, M. Kaneda, T. Hayakawa, H. Tsuchida, and A. Itoh, Nucl. Instrum. Methods Phys. Res. B **267**, 2667 (2009).
[16] M. Shimizu, T. Hayakawa, M. Kaneda, H. Tsuchida, and A. Itoh, Vacuum **84**, 1002 (2010).
[17] T. Siiskonen, H. Kettunen, K. Peräjärvi, A. Javanainen, M. Rossi, W. H. Trzaska, J. Turunen, and A. Virtanen, Phys. Med. Biol. **56**, 2367 (2011).
[18] M. Dingfelder, M. Inokuti, and H. G. Paretzke, Radiat. Phys. Chem. **59**, 255 (2000).
[19] A. Akkerman, A. Breskin, R. Chechik, and Y. Lifshitz, Radiat. Phys. Chem. **61**, 333 (2001).
[20] H. Date, K. L. Sutherland, T. Hayashi, Y. Matsuzaki, and Y. Kiyanagi, Radiat. Phys. Chem. **75**, 179 (2006).
[21] D. Emfietzoglou, R. Garcia-Molina, I. Kyriakou, I. Abril, and H. Nikjoo, Phys. Med. Biol. **54**, 3451 (2009).
[22] R. Garcia-Molina, I. Abril, C. D. Denton, S. Heredia-Avalos, I. Kyriakou, and D. Emfietzoglou, Nucl. Instrum. Methods Phys. Res. B **267**, 2647 (2009).
[23] R. Garcia-Molina, I. Abril, P. de Vera, and H. Paul, Nucl. Instrum. Methods Phys. Res. B **299**, 51 (2013).
[24] Z. Tan, Y. Xia, M. Zhao, X. Liu, F. Li, B. Huang, and Y. Ji, Nucl. Instrum. Methods Phys. Res. B **222**, 27 (2004).
[25] ICRU, Stopping Powers and Ranges for Protons and Alpha Particles, Report 49, Bethesda, MD, 1992.
[26] M. J. Berger, J. S. Coursey, M. A. Zucker, and J. Chang, ESTAR, PSTAR, and ASTAR: Computer programs for calculating stopping power and range tables for electrons, protons, and helium ions (version 1.2.3). Available from http://physics.nist.gov/Star (National Institute of Standards and Technology, Gaithersburg, MD, 2005).
[27] A. M. Koehler, J. G. Dickinson, and W. M. Preston, Rad. Res. **26**, 334 (1965).
[28] T. Hiraoka, K. Kawashima, K. Hoshinojan, and H. Bichsel, Phys. Med. Biol. **39**, 983 (1994).
[29] A. K. Nair, A. Gautieri, S.-W. Chang, and M. J. Buehler, Nat. Commun. **4**, 1724 (2013).
[30] ICRU, Photon, electron, proton and neutron interaction data for body tissues, Report 46, Bethesda, MD, 1992.
[31] P. Fratzl, H. S. Gupta, E. P. Paschalis, and P. Roschger, J. Mater. Chem. **14**, 2115 (2004).
[32] I. Yohannes, D. Kolditz, O. Langner, and W. A. Kalender, Phys. Med. Biol. **57**, 1173 (2012).
[33] A. C. Bento, D. P. Almond, S. R. Brown, and I. G. Turner, J. Appl. Phys. **79**, 6848 (1996).
[34] R. Astala and M. J. Stott, Phys. Rev. B **78**, 075427 (2008).
[35] M.-J. Lee, S.-K. Sohn, K.-T. Kim, C.-H. Kim, H.-B. Ahn, M.-S. Rho, M.-H. Jeong, and S.-K. Sun, Clin. Orthop. Surg. **2**, 90 (2010).
[36] P. Eddisford, A. Brown, and R. Brydson, J. Phys.: Conf. Ser. **126**, 012008 (2008).
[37] J. Reyes-Gasga, R. Garcia-Garcia, and E. Brès, Physica B **404**, 1867 (2009).
[38] L. L. Haas and G. H. Sandberg, Brit. J. Radiol. **30**, 19 (1957).
[39] H. Paul, O. Geithner, and O. Jakel, Adv. Quantum Chem. **52**, 289 (2007).
[40] M. Inokuti, Rev. Mod. Phys. **43**, 297 (1971); Addenda **50**, 23 (1978).
[41] A. Besemer, H. Paganetti, and B. Bednarz, Phys. Med. Biol. **58**, 887 (2013).
[42] I. Abril, R. Garcia-Molina, C. D. Denton, F. J. Pérez-Pérez, and N. R. Arista, Phys. Rev. A **58**, 357 (1998).
[43] S. Heredia-Avalos, R. Garcia-Molina, J. M. Fernández-Varea, and I. Abril, Phys. Rev. A **72**, 052902 (2005).
[44] R. Garcia-Molina, I. Abril, S. Heredia-Avalos, I. Kyriakou, and D. Emfietzoglou, Phys. Med. Biol. **56**, 6475 (2011).
[45] E. Mavropoulos, M. Hausen, A. M. Costa, G. Alves, A. Mello, C. A. Ospina, M. Mir, J. M. Granjeiro, and A. M. Rossi, J. Mater. Sci.: Mater. Med. **24**, 1271 (2013).

[46] Z. Hong, L. Luan, S.-B. Paik, B. Deng, D. E. Ellis, J. B. Ketterson, A. Mello, J. G. Eon, J. Terra, and A. M. Rossi, Thin Solid Films **515**, 6773 (2007).
[47] A. Mello, Z. Hong, A. M. Rossi, L. Luan, M. Farina, W. Querido, J. Eon, J. Terra, G. Balasundaram, T. Webster, A. Feinerman, D. E. Ellis, J. B. Ketterson, and C. L. Ferreira, Biomed. Mater. **2**, 67 (2007).
[48] Z. Hong, A. Mello, T. Yoshida, L. Luan, P. H. Stern, A. Rossi, D. E. Ellis, and J. B. Ketterson, J. Biomed. Mater. Res. A **93A**, 878 (2010).
[49] L. G. Parratt, Phys. Rev. **95**, 359 (1954).
[50] L. C. C. M. Nagamine, A. Biondo, L. G. Pereira, A. Mello, J. E. Schmidt, T. W. Chimendes, J. B. M. Cunha, and E. B. Saitovitch, J. Appl. Phys. **94**, 5881 (2003).
[51] E. O. Lopez, A. Mello, H. Sendao, L. T. Costa, A. L. Rossi, R. O. Ospina, F. F. Borghi, J. G. S. Filho, and A. M. Rossi, ACS Appl. Mater. Interfaces **5**, 9435 (2013).
[52] M. Behar, R. C. Fadanelli, I. Abril, R. Garcia-Molina, C. D. Denton, L. C. C. M. Nagamine, and N. R. Arista, Phys. Rev. A **80**, 062901 (2009).
[53] W. K. Chu, J. W. Mayer, and M. A. Nicolet, *Backscattering Spectrometry* (Academic, New York, 1978).
[54] J. Lindhard, Dan. Mat. Fys. Medd. **28**, No. 8 (1954).
[55] R. H. Ritchie, Phys. Rev. **106**, 874 (1957).
[56] H. Nikjoo, S. Uehara, and D. Emfietzoglou, *Interaction of Radiation With Matter* (CRC, Boca Raton, FL, 2012).
[57] W. Brandt and M. Kitagawa, Phys. Rev. B **25**, 5631 (1982).
[58] W. Brandt, Nucl. Instrum. Methods **194**, 13 (1982).
[59] G. Schiwietz and P. L. Grande, Nucl. Instrum. Methods Phys. Res. B **175–177**, 125 (2001).
[60] R. F. Egerton, *Electron Energy-Loss Spectroscopy in the Electron Microscope* (Plenum, New York, 1989).
[61] N. D. Mermin, Phys. Rev. B **1**, 2362 (1970).
[62] R. Garcia-Molina, I. Abril, I. Kyriakou, and D. Emfietzoglou, in *Radiation Damage in Biomolecular Systems*, edited by G. Garcia Gomez-Tejedor and M. C. Fuss (Springer, Dordrecht, 2012), Chap. 15.
[63] I. Abril, R. Garcia-Molina, P. de Vera, I. Kyriakou, and D. Emfietzoglou, Adv. Quantum Chem. **65**, 129 (2013).
[64] P. Rulis, L. Ouyang, and W. Y. Ching, Phys. Rev. B **70**, 155104 (2004).
[65] D. Y. Smith and E. Shiles, Phys. Rev. B **17**, 4689 (1978).
[66] B. L. Henke, E. M. Gullikson, and J. C. Davis, Atomic Data Nucl. Data Tables **54**, 181 (1993).
[67] J. F. Ziegler, J. P. Biersak, and M. D. Ziegler, *SRIM. The Stopping and Range of Ions in Matter* (SRIM, Chester, MD, 2008).
[68] U. Fano, Annu. Rev. Nucl. Sci. **13**, 1 (1963).
[69] P. de Vera, I. Abril, and R. Garcia-Molina, J. Appl. Phys. **109**, 094901 (2011).
[70] R. Garcia-Molina, I. Abril, P. de Vera, I. Kyriakou, and D. Emfietzoglou, in *Fast Ion-Atom and Ion-Molecule Collisions*, edited by D. Belkic (World Scientific, Singapore, 2012), Chap. 8.
[71] G. Ciangaru, J. C. Polf, M. Bues, and A. R. Smith, Med. Phys. **32**, 3511 (2005).
[72] S. C. Cardoso, V. G. L. Alves, L. A. R. da Rosa, L. T. Campos, D. V. S. Batista, and A. Facure, PLoS ONE **5**, e10466 (2010).